Influence of the Nanostructure of Palladium Mesoparticles on the Kinetics of Molecular Oxygen Electroreduction

A. Hernández Creus,[†] Y. Gimeno,[†] P. Díaz,[†] L. Vázquez,[‡] S. González,[†] R. C. Salvarezza,[§] and A. J. Arvia*[,§]

Departamento de Química Física, Universidad de la Laguna, Spain, Instituto de Investigaciones Fisicoquímicas Teóricas y Aplicadas, Universidad Nacional de La Plata−CONICET, Sucursal 4 Casilla de Correo 16 (1900) La Plata, Argentina, and Instituto de Ciencia de Materiales de Madrid, Consejo Superior de Investigaciones Científicas, Cantoblanco, 28049 Madrid, Spain

Received: November 18, 2003; In Final Form: March 23, 2004

The effect of the nanostructure of electrodeposited palladium mesoparticles on the oxygen electroreduction reaction (oerr) in acid media is studied by electrochemical techniques combined with scanning tunneling microscopy, tapping-mode atomic force microscopy, and scanning electron microscopy. Palladium mesoparticles supported on highly oriented pyrolytic graphite (HOPG) exhibit a remarkable electrocatalytic enhancement, i.e., a decrease in the cathodic overvoltage on the order of 0.25 V, as compared to polycrystalline palladium electrodes. For a similar particle size, the largest electrocatalytic activity is obtained by use of quasi-two-dimensional (2D) ramified palladium particles and electrodeposited palladium charges exceeding 3 mC cm^{-2}. For these particles, experimental results show that the electrocatalytic enhancement of the oerr can be related to the combined influence of the nanostructure of 2D branching on the HOPG and traces of oxygen-containing adsorbates that induces local perturbation of electronic states at palladium mesoparticles. The 2D nature of surfaces increases markedly the reversibility of the first two-electron-transfer step of the oerr.

1. Introduction

Metal nano/mesoparticles are of interest due to their unique physical, chemical, and electrochemical properties, making them of importance in many technical applications. Noble metal islands at the nanometer to micrometer range have been produced on different substrates to be used in heterogeneous catalysis and electrocatalysis. These materials have attracted great interest due to their potential applicability in relation to fundamental aspects of electrochemistry[1] and to many reactions of both industrial and environmental importance.[2−4]

In recent years a great effort has been made to attain a predictive understanding of the relationship between the shape and structure of metal particles of low dimensionality and their catalytic activity. Significant progress in this direction has been made showing that the high activity requires a minimum metal particle size that should be compatible with bulk physicochemical properties of metal nano/mesoparticles. The latter also depends to a large extent on the large area/volume atomic ratio of these particles as compared to bulk metals. In contrast to this progress, the fabrication of metal nano/mesoparticles still remains rather empirical because some fundamental aspects of those processes yielding particles with preselected dimensionality, shape, and size at the nanometer scale are not fully dominated.

Metal nano/mesoparticles can be prepared by different techniques such as vapor deposition, ultrahigh vapor deposition, chemical vapor deposition, electroless deposition, chemical impregnation methods, lithographic methods, homogeneous reactions in solution and electrodeposition. In principle, metal electrodeposition appears to be a promising choice for producing nano/mesoparticles because the experimental variables that determine the growth mode, at least on well-defined substrates, are rather easy to control. For instance, in metal electrodeposition, by adjusting the operation variables adequately, it is possible to modify the kinetics of the electrochemical reactions from surface- to a mass transport-controlled kinetics. Accordingly, the production of metal nano/mesoparticles by electrodeposition on well-defined conducting substrates offers the possibility of investigating the influence of operating variables on dimensionality, particle size, and structure. The catalytic properties of these particles can be determined by conventional elecrocatalytic test reactions.

Carbon-supported palladium catalysts are utilized in a number of heterogeneous chemical hydrogenation and oxidation reactions, electrocatalytic reactions, and, due to their increased sensitivity, also for electroanalytical reactions.[5] The sorptive and catalytic properties of palladium electrodeposits on platinum, as well as the composition of α-phase palladium hydride on platinum and carbon, depend on the electrodeposition potential,[6−8] particularly when the phase growth is accompanied by deep hydrogenation of palladium.[9] The scale-dependent structure and surface properties of palladium particles grown on a variety of substrates are related to the growth mode of the deposit. Therefore, it is interesting to establish the optimal range of electrodeposition potential (E_d) and electrolysis time (t_d) associated with certain characteristics of palladium meso/nanostructures of interest for applications in optics, catalysis, and electrocatalysis.

Palladium-modified carbon electrodes can be prepared by different techniques, namely, by soaking the substrate into

* To whom correspondence may be addressed. E-mail: ajarvia@inifta.unlp.edu.ar.
[†] Universidad de la Laguna.
[‡] Instituto de Ciencia de Materiales de Madrid, CSIC.
[§] Universidad Nacional de La Plata−CONICET.

10.1021/jp0375214 CCC: $27.50
Published on Web 06/23/2004

palladium ion-containing solutions followed by adequate baking to reduce palladium compound to palladium; by vapor-phase palladium deposition, and by electrodeposition from a palladium plating solution onto different conducting substrates.[10] Recently, we described a potentiostatic method to produce palladium mesoislands of different geometry on highly oriented pyrolytic graphite (HOPG) by electrodeposition from aqueous palladium plating acid solutions.[11,12] These palladium islands, either quasi-cylindrical (type I) or branched (type II), can be easily obtained, their size depending on the electrodeposition charge (q_d) and their shape being determined by selecting the potential window from the cathodic polarization curve. These palladium mesoislands exhibited an electrocatalytic enhancement for both the complete electro-oxidation of hydrazine and the hydrogen adsorption/desorption processes. For these reactions palladium islands of type II were the most effective ones.

The oxygen electroreduction reaction (oerr) in aqueous environments is one of the most important processes in nature, covering from biological systems to technical applications such as metal corrosion and fuel cell technology.[13] In acid solution, the overall oxygen electrode reaction is represented by

$$O_2(g) + 4H^+(aq) + 4e^- = 4H_2O \qquad (1)$$

Reaction 1 on noble metal electrodes is a complex reaction with a relatively high cathodic overvoltage. An important task in electrocatalysis is to discover new materials and electrode designs for diminishing the cathodic overvoltage of the process as much as possible. The kinetics of the oerr on bulk palladium in acid solution is characterized by a cathodic overvoltage versus log (cathodic current density) linear relationship with a Tafel slope equal to -0.12 V/decade.[14−16] The reaction occurs on a "bare" palladium cathode and its kinetics is determined by the first two-electron-transfer steps in which hydrogen peroxide is formed.

As has been recently reported,[17] the cathodic overvoltage of the oerr on a gold substrate covered by a palladium submonolayer with a degree of surface coverage $\theta \cong 0.9$ decreases markedly in relation to that of a "bare" gold electrode. Furthermore, an outstanding electrocatalytic activation for reaction 1 on gold nanoparticles supported on gold has been reported.[18,19] The behavior of the oerr on gold nanoelectrodeposits on boron-doped diamond films also exhibit a quasireversible electroreduction wave on gold modified by a self-assembled submonolayer of cysteine.[20]

In this work we report the electrocatalytic enhancement of both the oerr and the hydrogen adatom formation in terms of palladium island size and geometry. The presence of quasi 2D domains that constitute these palladium islands appears to be largely responsible for the above effect. This conclusion emerges from the analysis of electrochemical data, scanning tunneling microscopy (STM), and tapping-mode atomic force microscopy (AFM) imaging and scanning electron microscopy (SEM) micrographs of the oerr on palladium electrodeposited patterns. The kinetics of the oerr palladium mesoparticles supported on highly oriented pyrolytic graphite (HOPG) exhibit a remarkable electrocatalytic enhancement, i.e., a decrease in the cathodic overvoltage on the order of 0.25 V, as compared to polycrystalline palladium electrodes. This fact suggests that the initial step would involve the possible enhancement of molecular oxygen dissociative adsorption on palladium island 2D domains. These findings establish a consistent bridge between the electrocatalytic activity of palladium islands and that found earlier for palladium electrodes previously subjected to electroroughening.[21,22]

2. Experimental Section

2.1. Preparation of Palladium Mesoislands on HOPG. Palladium islands on freshly exfoliated HOPG working electrodes (geometric area 0.55 cm^2) were grown by electrodeposition from 7.5×10^{-4} M palladium chloride + 5×10^{-2} M sodium perchlorate + 5×10^{-3} M perchloric acid aqueous solution utilizing a conventional glass electrochemical cell provided with a palladium counter electrode and a saturated calomel electrode (SCE) as the reference. The working solution was prepared from analytical reagent-grade chemicals and Milli-Q*-Millipore water and deaerated by bubbling with purified argon prior to each electrochemical run.

Potentials in the text are referred to the SCE scale. The working conditions to establish the optimal growth mode for palladium branched islands were evaluated from a cathodic polarization curve run at 0.005 V/s between an anodic switching potential in the range $0.7 \le E_{as} \le 0.8$ V and a cathodic switching potential in the range where the discharge of hydrogen ions takes place. The reversible potential of the $Pd/Pd^{2+}(aq)$ electrode for the working solution is $E_r = 0.74$ V (versus SCE) at 298 K.[23]

As concluded from polarization curves, palladium islands were grown by stepping the potential from $E_i = 0.7$ V to a value of E_d set in the range -0.100 V $\le E_d \le 0.125$ V. The electrodeposition time was set in the range $10 \le t_d \le 650$ s. The electrodeposition charge density that was determined with a digitalized coulometer was in the range $1 \le q_d \le 12$ mC cm^{-2}. Values of the cathodic current density (j) and q_d are referred to the geometric area of the HOPG substrate. Depending on the value of E_d, two types of palladium islands were prepared, being denoted as type I ($E_d \approx 0.125$ V) and type II palladium islands ($E_d \approx -0.100$ V) on HOPG (hereafter referred to as type I and type II palladium, respectively). Occasionally, a part of the electrodeposited palladium was anodically stripped off to decrease the average island size and later determine how their electrocatalytic activity was modified.

2.2. Surface Characterization. The surface characterization of palladium islands on HOPG working electrodes was made by STM, AFM, and SEM. For this purpose the working electrode was removed from the cell, carefully rinsed by immersion in water for 2 min, and dried under argon at room temperature.

SEM micrographs were obtained on JEOL equipment. STM images were produced from a Nanoscope IIE digital instrument operating in air. Tapping-mode AFM images were made with a Nanoscope IIIa digital instrument operating under water.

For STM imaging, Pt−Ir Nanotips were used. Tunneling currents in the range 0.5−0.8 nA and bias voltages in the range 0.5−1.0 V were used. Images were taken at a low scan rate ($\approx$0.8 Hz for images 5×5 μm^2 in size) to avoid either damage of the deposit or its removal from the HOPG surface by the tip.

Because of the weak attachment of palladium islands to the graphite surface, we used tapping-mode AFM in an underwater environment to avoid material stripping. This made repetitive imaging of palladium islands possible. These measurements were performed with silicon nitride cantilevers at a resonance frequency close to 10 kHz. Set points close to the free oscillation amplitudes were employed to minimize the cantilever−palladium island interaction.

2.3. Electrocatalytic Properties. The electrocatalytic activity of type I and type II palladium supported on HOPG electrodes for the oerr in oxygen-saturated 0.05 M aqueous perchloric acid was determined voltammetrically at $\nu = 0.050$ V s^{-1}. For comparison, blanks were run for both bare HOPG and massive

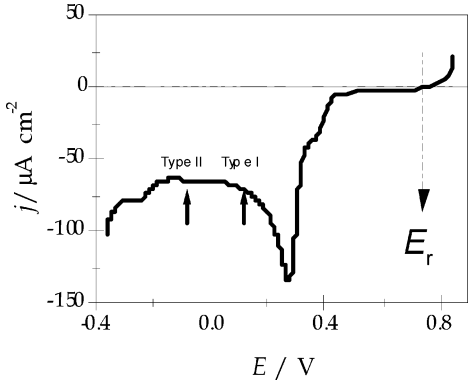

Figure 1. Cathodic polarization curve at 5×10^{-3} V s^{-1}. HOPG in 7.5×10^{-4} M aqueous $PdCl_2 + 5 \times 10^{-2}$ M $NaClO_4 + 5 \times 10^{-3}$ M $HClO_4$; 298 K. The current density (j) is referred to the working electrode geometric area. The reversible potential of the Pd/Pd^{2+} electrode in the working solution and the potentials for the preparation of type I and type II palladium are indicated.

palladium electrodes. All experiments were performed at 298 K. It should be pointed out that voltammetry provides relevant kinetic information about the oerr; however, from the standpoint of practical application to electrocatalysis, data for the process under steady-state conditions are required.

3. Results

3.1. Palladium Island Preparation. The cathodic polarization curve of palladium electrodeposition on HOPG run from 0.8 to −0.4 V, at 0.005 V/s, plotted as cathodic current density (j) versus applied potential (E) (Figure 1), shows the following features. From 0.8 to ca. 0.4 V there is an almost exponential increase in j with E. Subsequently, a tendency to attain a first limiting current in the range 0.4−0.3 V was observed. This current was followed by a cathodic current maximum at 0.27 V and a second cathodic limiting current that extends from ca. 0 to −0.2 V. These current contributions are related to the discharge of aqueous palladium complex species to palladium. Finally, from −0.2 V downward, the simultaneous electrodeposition of palladium and the discharge of hydrogen ions take place. The kinetics of these processes has been extensively discussed in a previous publication.[12] The potential regions related to the preparation of type I and type II palladium islands are indicated in Figure 1.

3.2. Palladium Island Characterization. Type I palladium (Figure 2a) appears as compact, cylindrical particles either isolated or as twinned and trimer islands. The average maximum island radius $\langle r \rangle$ is close to 100 nm (Figure 2b), and the maximum height/maximum radius ratio $\langle h \rangle / \langle r \rangle = f$ is about 0.32 (Figure 2b,c). On the other hand, type II palladium involving the same value of q_d (Figure 3a) consists of a small central 3D core surrounded by large and flat branches (Figure 3b). In this case, for $q_d = 3$ mC/cm^2, $\langle f \rangle$ is 0.25 (Figure 3c). The island patterns for type I and type II palladium resulting from the cross-section analysis (Figures 2c and 3c) are completely different. In fact, for type II palladium the branched pattern around the small central core is extremely flat with a maximum height close to 5 nm that corresponds to about 20 monolayers (ML) of palladium atoms, i.e., it approaches a real 2D pattern as shown in Figure 3c. Both type I and type II palladium exhibit a narrow particle size distribution with an average radius $\langle r \rangle$ and an average height $\langle h \rangle$ both increasing with q_d, fulfilling linear relationships $\langle h \rangle \propto q_d^m$ and $\langle r \rangle \propto q_d^n$, respectively, with $m = 0.15$ and $n = 0.40$ (Figure 4).[21] Accordingly, as palladium islands grow they tend to spread over the HOPG surface, leading to smaller values of $\langle f \rangle$. For both type I and type II palladium, percolation patterns at high values of q_d can be formed, although for type II palladium, the high connectivity of branches results in percolation patterns that can already be observed at $q_d \approx 6$ mC cm^{-2}.

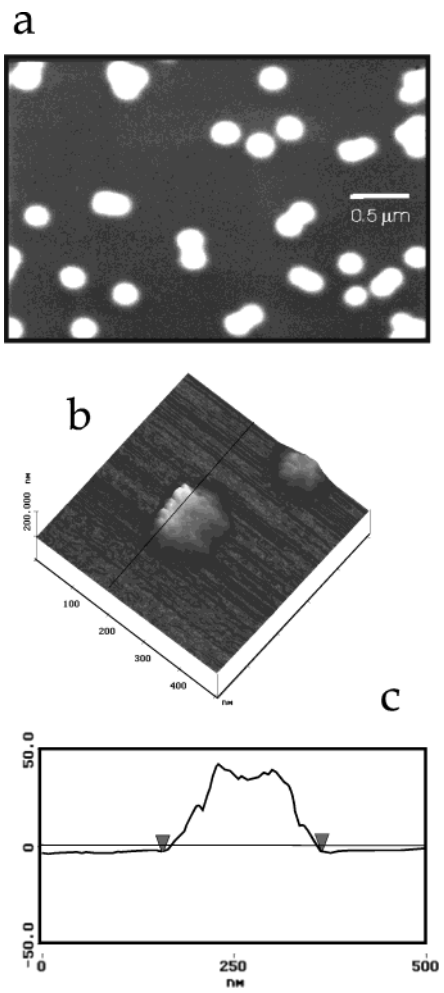

Figure 2. Type I palladium. (a) SEM micrograph, $q_d = 5$ mC cm^{-2}. (b) STM image (0.5×0.5 μm^2), $q_d = 3$ mC cm^{-2}. (c) STM cross section of the image shown in panel b.

3.3. Electrocatalysis (oerr) on Palladium Mesoparticles Supported on HOPG. Polarization curves from oxygen-saturated 0.05 M aqueous perchloric acid on bare HOPG, massive palladium, and type II palladium ($q_d = 3$ mC cm^{-2}) were run at 0.050 V s^{-1}, increasing the potential scan from 0.45 to 0.70 V and reversing it to −0.2 V (Figure 5). As already reported,[16] the initial potential scan from 0.45 to 0.70 V considerably improves the reproducibility of the oxygen electroreduction curves.

The polarization curve on bare HOPG (blank) (Figure 5) shows that the electroreduction current becomes negligible as only a small cathodic wave in the range 0 to −0.1 V, presumably associated with the charging/discharging current of the electrical double layer, is recorded. For $E < 0$ V, the discharge of hydrogen ions contributes to the gradual increase in j as E is negatively shifted.

The cathodic polarization curves for massive palladium (Figure 5) run under comparable conditions exhibit a first exponential increase in current from 0.6 to 0.2 V, followed by a diffusion-controlled current plateau related to the oerr from 0.1 to 0 V. The increase in current from 0 V downward corresponds to the contribution of the hydrogen ion discharge reaction.

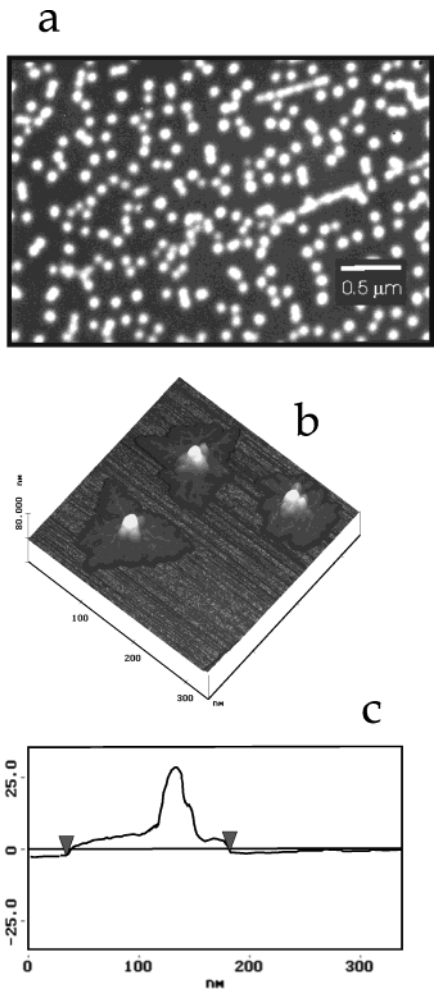

Figure 3. Type II palladium. (a) SEM micrograph, $q_d = 5$ mC cm^{-2}. (b) STM image (0.32 × 0.32 μm^2), $q_d = 3$ mC cm^{-2}. (c) STM cross section of the image shown in panel b.

A comparable polarization curve run with type II palladium in the oxygen-saturated working solution shows two cathodic waves in the potential ranges 0.32 to 0.20 and 0.15 to −0.05 V (Figure 5). These two waves are related to the oerr as they disappear when the polarization curve is recorded in oxygen-free 0.05 M aqueous perchloric acid. For $E < -0.1$ V, the current contribution from the hydrogen ion discharge is observed. However, in contrast to massive palladium, in which the hydrogen ion discharge leading to hydrogen absorption is the dominant process, for type II palladium the hydrogen ion discharge involves a current plateau at −0.12 V. This behavior is similar to that earlier described for electroroughened massive palladium[21,22] and attributed to the discharge of hydrogen ions principally yielding electroadsorbed hydrogen atoms.

The above results demonstrate that the cathodic overvoltage for the oerr on type II palladium in aqueous perchloric acid decreases by 0.21 V as compared to massive palladium. It should be noted that the cathodic current density referred to 1 cm^2 of HOPG for both type II palladium and massive palladium is almost the same, despite the fact that in the former case dispersed islands on HOPG involve only a few micrograms of palladium.

For both type I and type II palladium, the polarization curves for the oerr run at 0.050 V/s show a gradual shift in the inflection point as q_d is increased from 1 to 6 mC cm^{-2} (Figure 6). The potential of the inflection point ($E_{1/2}$) is used as a measure of the shift in the cathodic overvoltage of the oerr. This shift is

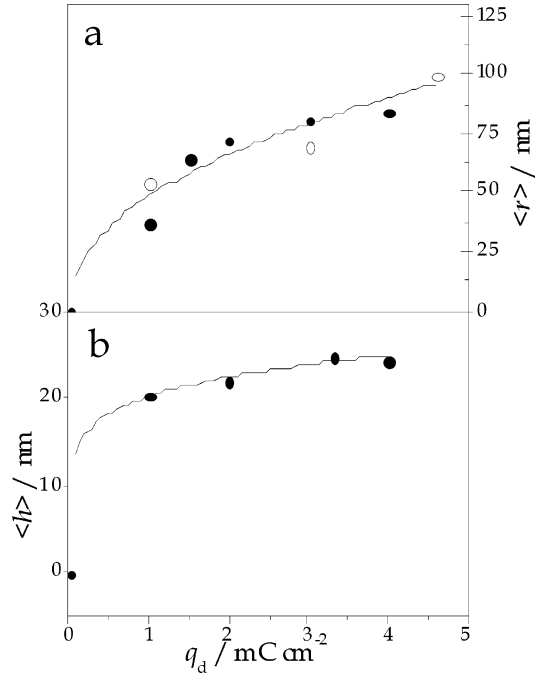

Figure 4. (a) Plot of $\langle r \rangle$ versus q_d. The solid line corresponds to $\langle r \rangle$ versus $q_d^{0.4}$. (b) Plot of $\langle h \rangle$ versus q_d. The solid line corresponds to $\langle h \rangle$ versus $q_d^{0.15}$. Type II palladium (●) and type I palladium (○) are shown.

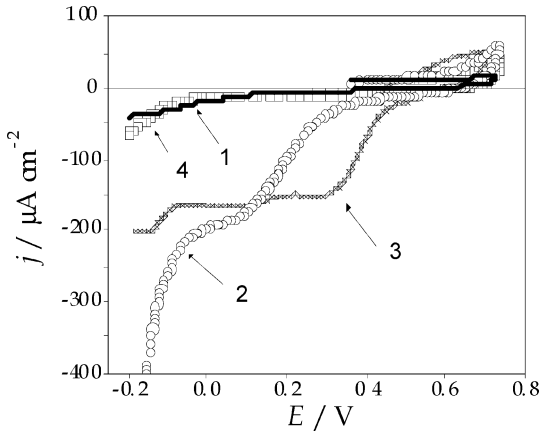

Figure 5. Polarization curves in 0.05 M aqueous perchloric acid run at $v = 0.050$ V s^{-1} from 0.45 to 0.70 V and backward to −0.20 V: HOPG in oxygen-saturated solution (■, 1); polycrystalline palladium in oxygen-saturated solution (○, 2); type II palladium ($q_d = 3$ mC cm^{-2}) in oxygen-saturated solution (∗, 3); and type II palladium ($q_d = 3$mC cm^{-2}) in a deaerated solution (□, 4).

acompanied by a monotonic increase in the hydrogen atom electroadsorption wave $E < 0$ V. It should be noted that the decrease in the cathodic overvoltage for the oerr for type II palladium is larger than for type I palladium. Therefore, type II palladium exhibits the largest electrocatalytic effect for the oerr. This conclusion is consistent with the fact that for both type I and type II palladium the experimental value of $E_{1/2}$ moves positively with q_d, although this effect is more remarkable for type II palladium (Figure 7). The $E_{1/2}$ versus q_d plot (Figure 7) clearly shows that the shift of $E_{1/2}$ with q_d reaches the equilibrium potential of the O_2/H_2O_2 redox couple as limiting value (Table 1). This means that the first electroreduction step of oxygen to hydrogen peroxide turns into a reversible process for $q_d \geq 5$ mC cm^{-2}. Accordingly, the electrocatalysis of type I and type II palladium seems to operate at the first electron-transfer step of the complex mechanism related to the oerr.[16]

TABLE 1: Reversible Potential of Reactions of Possible Interest for the Molecular Oxygen Electroreduction Reaction[a]

equilibrium reaction	E_0/V	Nernst equation	E_r/V
$O(g) + 2H^+ + 2e^- = H_2O$	2.162	$E_r/V = 2.162 - 0.059pH + 0.030 \log p_O$	≈2.085
$H_2O_2 + 2H^+ + 2e^- = 2H_2O$	1.495	$E_r/V = 1.459 - 0.059pH + 0.030 \log c_{H2O2}$	1.576
$O_2(g) + 4H^+ + 4e^- = 2H_2O$	0.961	$E_r/V = 0.961 - 0.059pH + 0.015 \log p_{O2}$	0.884
$O_2(g) + 2H^+ + 2e^- = H_2O_2$	0.427	$E_r/V = 0.427 - 0.059pH + 0.030 \log p_{O2} - 0.030 \log c_{H2O2}$	0.508
$Pd^{2+}(aq) + 2\ e^- = Pd(s)$	0.647	$E_r/V = 0.647 - 0.030 \log c_{Pd2+}$	0.741

[a] Potentials are referred to the potential of the saturated calomel electrode (versus the normal hydrogen electrode). Data are adapted from ref 23 and were measured at 298 K.

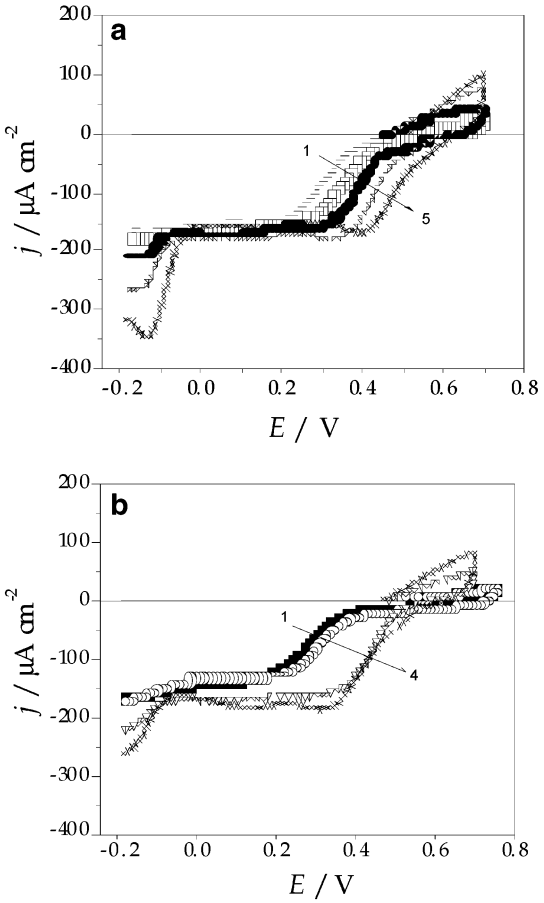

Figure 6. Polarization curves for the oerr in 0.05 M aqueous perchloric acid at $\upsilon = 0.050$ V s^{-1} run in oxygen-saturated solution run from 0.45 to 0.70 V and backward to −0.20 V. (a) Type II palladium (q_d = 1, 2, 3, 6, and 12 mC cm^{-2}). (b) Type I palladium (q_d = 2, 3, 6, and 12 mC cm^{-2}). The arrow indicates the charge density increasing direction.

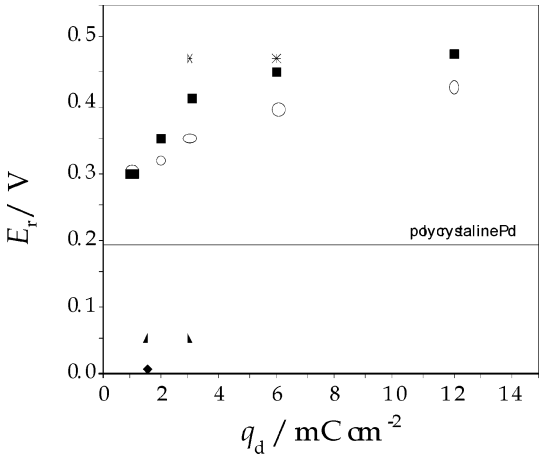

Figure 7. Plot of $E_{1/2}$ versus q_d from polarization curves run in oxygen-saturated 0.05 M aqueous perchloric acid at $\upsilon = 0.050$ V s^{-1}. (■) Type II palladium; (○) type I palladium; (—) polycrystalline palladium; (▲) type III palladium; (◆) HOPG; (∗) palladium nanoparticles electrodeposited on gold (111) at $E_d = -0.1$ V.

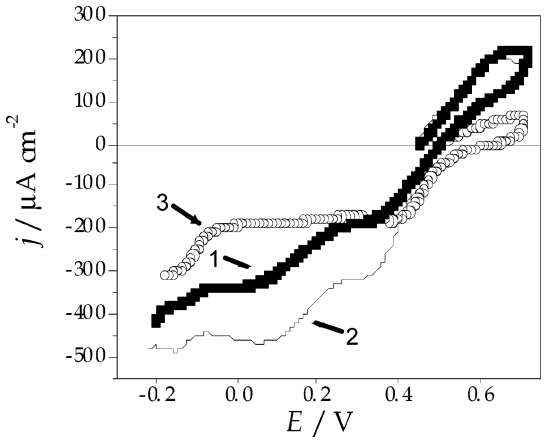

Figure 8. Polarization curves for type II palladium (q_d = 6 mC cm^{-2}) in 0.05 M aqueous perchloric acid run at $\upsilon = 0.050$ V s^{-1} from 0.45 to 0.70 V before the electroreduction scan. Deaerated solution + 3.53 × 10^{-6} M H_2O_2 (■, 1); oxygen-saturated solution + 3.53 × 10^{-6} M H_2O_2 (—, 2); oxygen-saturated solution (○, 3).

To demonstrate the validity of the above conclusions, runs under comparable conditions were made with type II palladium (q_d = 6 mC/cm^2) in the oxygen-saturated working solution with the addition of 3.5 × 10^{-6} M hydrogen peroxide. The corresponding voltammogram (Figure 8, —) shows two successive cathodic waves, one with $E_{1/2} = 0.42$ V, a value approaching that of the $O_2/H_2O_2/2e^-$ reversible potential, and the other $E_{1/2} = 0.18$ V, that resembles the single wave found for massive palladium (Figure 5). These two waves are also present in the voltammogram run in the absence of hydrogen peroxide (Figure 8, ○). The relative increase in the charge of the cathodic waves observed for the solution containing hydrogen peroxide appears to be also related to the application of the initial positive potential scan from 0.4 to 0.7 V. This initial scan produces an additional local supersaturation of oxygen resulting from the electro-oxidation of a certain amount of hydrogen peroxide. On the other hand, when oxygen is removed from the hydrogen peroxide-containing solution only the wave at 0.18 V is observed, i.e., this second wave is related to the electroreduction of hydrogen peroxide itself. Therefore, these results provide useful information to interpret the kinetics and mechanism of the oerr on type I and type II palladium as discussed further on.

Another electrocatalytic effect that appears in the voltammograms for both type I and type II palladium is related to the formation of electroadsorbed hydrogen atoms from the discharge of hydrogen ions. This is reflected in the cathodic current (j_{haer}) recorded for $E < 0$ V, which is not observable for massive mirror-polished palladium (Figure 5). For both types of electrodes the ($j_{haer} - j_{limO_2}$) versus q_d plots (Figure 9) yield reasonable straight lines, although for type II palladium the slope of this line is greater than for type I palladium. Considering

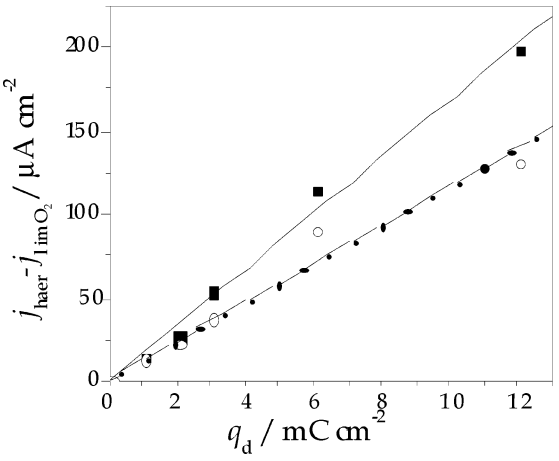

Figure 9. Plots of ($j_{haer} - j_{limO_2}$) versus q_d for type II palladium (■) and type I palladium (○).

that the real surface area of type II palladium is larger than for type I palladium, this behavior suggests that for $E < 0$ V the dominant reaction corresponds to a surface process in which the hydrogen ion discharge yields hydrogen adatoms on palladium as precursors of hydrogen absorption into bulk palladium. This electrochemical behavior is similar to that already reported for electrochemically roughened palladium electrodes.[21,22] For the same value of q_d, these plots also indicate that the degree of surface coverage of palladium by hydrogen atoms becomes slightly greater for type II than for type I palladium.

The preceding results suggested the need for a crucial experiment to demonstrate whether the catalytic activity of type I and type II palladium is due preferentially to either the island size or dominant island geometry. For this purpose, a type II palladium ($q_d = 3$ mC cm^{-2}) exhibiting a high electrocatalytic activity for the oerr was anodically stripped off, leaving just half of the initial palladium electrodeposition charge ($q_d = 1.5$ mC cm^{-2}). Hereafter this type of electrode is denoted as type III palladium. After anodic stripping, the tapping-mode AFM image shows extremely disordered patterns (Figure 10), consisting of central cores and backbones of the original branched pattern, i.e., the 2D branching from the initial palladium electrodeposit was almost completely removed by partial anodic stripping leading to a quasi-1D branched pattern. The electrocatalytic behavior of these quasi-1D palladium islands for the oerr on HOPG was also tested (Figure 11). The comparison of data from type II palladium ($q_d = 3$ mC cm^{-2}) to that of quasi-1D palladium prepared from type II palladium ($q_d = 6$ mC cm^{-2}) after anodic stripping to $q_d = 3$ mC cm^{-2} reveals that for the latter the electrocatalytic effect on the oerr has disappeared almost completely, i.e., the corresponding value of $E_{1/2}$

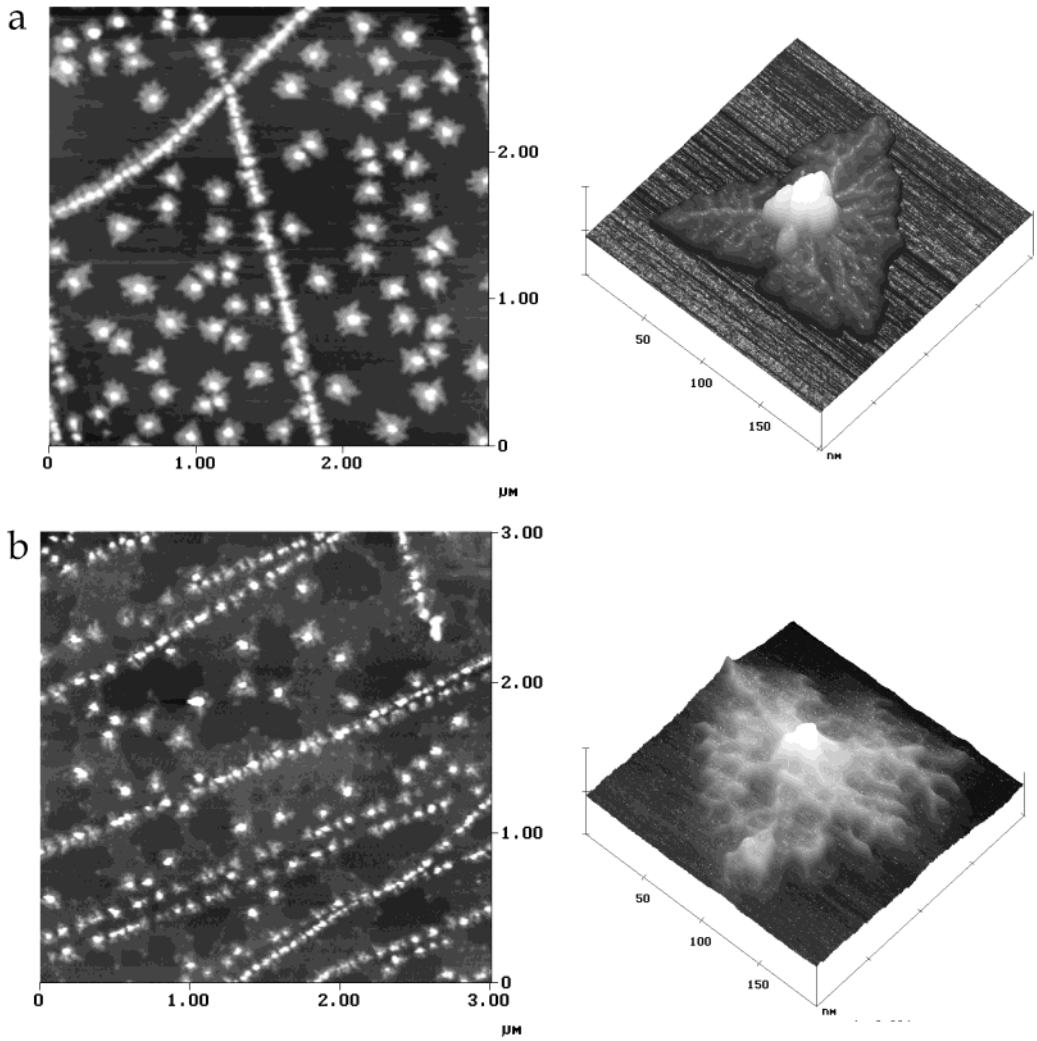

Figure 10. Imaging comparison between type II and type III palladium. (a) STM image of type II palladium ($q_d = 3$ mC cm^{-2}); (b) tapping-mode AFM image of type III palladium ($q_d = 1.5$ mC cm^{-2} resulting from the anodic stripping of type II palladium with the initial value $q_d = 3$ mC cm^{-2}).

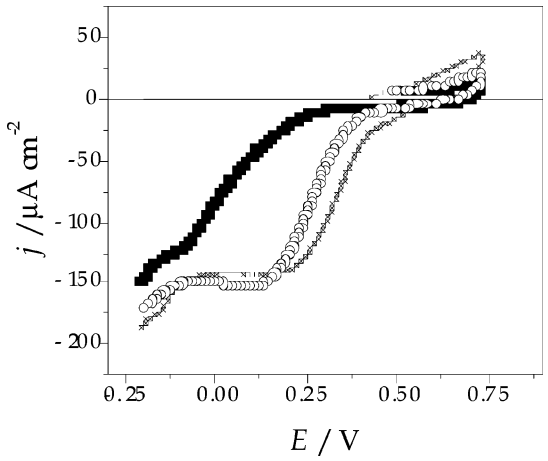

Figure 11. Polarization curves run in 0.05 M aqueous perchloric acid at $v = 0.050$ V s^{-1} from 0.45 to 0.70 V before the electroreduction scan. Oxygen-saturated solution. Type I palladium ($q_d = 3$ mC cm^{-2}) (○); type II palladium ($q_d = 3$ mC cm^{-2}) (∗); type III palladium ($q_d = 3$ mC cm^{-2} resulting from the anodic stripping of from the initial value $q_d = 6$ mC cm^{-2}) (■).

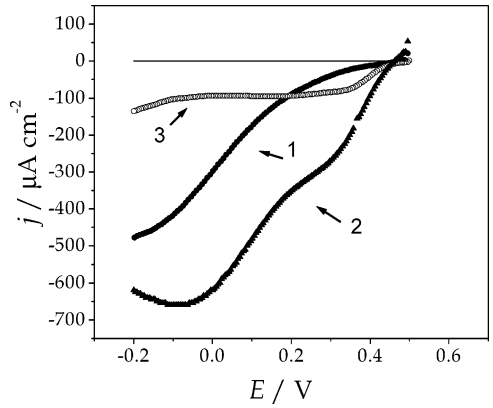

Figure 12. Polarization curves run at $v = 0.050$ V s^{-1} in 0.05 M aqueous perchloric acid for type II palladium ($q_d = 6$ mC cm^{-2}) from 0.50 to −0.20 V: deaerated solution with 3.53×10^{-6} M H_2O_2 (curve 1); oxygen-saturated solution + 3.53×10^{-6} M H_2O_2 (curve 2); oxygen-saturated solution (curve 3).

approaches that resulting from the HOPG blank (Figure 7). In this case, the oerr behaves as an irreversible electrochemical surface reaction, although the electrocatalytic effect on the hydrogen electroadsorption reaction remains and resembles that observed for type I palladium.

To investigate the influence of possible oxygen−substrate surface interactions on the oerr, polarization curves for type II palladium ($q_d = 6$ mC cm^{-2}) were run starting from 0.5 V downward (Figure 12). In this case, the relative contribution of any oxygen-containing surface species is largely diminished as compared to polarization conditions used in those runs depicted in Figure 8. For type II palladium in oxygen-saturated 0.05 M aqueous perchloric acid, oxygen-saturated 0.05 M aqueous perchloric acid + hydrogen peroxide, and oxygen-free hydrogen peroxide (Figure 12), the most remarkable effect as compared to Figure 8 is the negative shift of the oerr threshold potential that indicates a decrease in the electrocatalytic effect for the oerr. The voltammogram for massive palladium in the acid solution (Figure 13) also shows that oxygen-containing adsorbed species on palladium are present in the potential range of the oerr. These results clearly demonstrate that traces of oxygen-containing adsorbates remaining on palladium species also contribute to the electrocatalytic enhancement of the oerr.

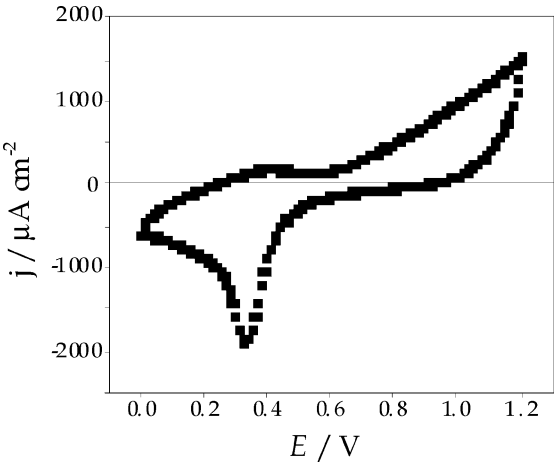

Figure 13. Voltammogram of polycrystalline palladium in deaerated aqueous 0.05 M aqueous perchloric acid.

To further investigate the influence of the substrate on the electrocatalysis of the oerr, voltammetric runs were also made under comparable conditions with a gold(111) substrate with different amounts of electrodeposited palladium in oxygen-saturated 0.05 M aqueous perchloric acid (Figure 14a). These voltammograms started with an electro-oxidation scan from 0.65 to 0.70 V, followed by the electroreduction scan downward to −0.2 V. In all cases, for $E \geq 0.50$ V, a cathodic current presumably related to the electroreduction of a submonolayer of oxygen-containing adsorbates (oxygen upd) anodically formed in the preceding scan was observed. In any case, the cathodic current starting from 0.50 V downward attains a limiting value from ca. 0.3 to 0.0 V. STM images of the electrodeposited palladium islands ($q_d = 3$ mC cm^{-2}) on gold consist of nanoparticles (10−20 nm in size, 1−2 nm in height) practically covering the entire gold surface (Figure 14b). The largest nanoparticles exhibit triangular and ramified shapes and others in which branch development is hindered by the overlapping of growing island borders. It should be noted that the effect of the substrate cannot be strictly derived from these experiments because both the substrate and the type of deposited islands have been simultaneously changed. In fact, under the same experimental conditions the nucleation rate of palladium on gold is much higher than on HOPG, resulting in a large number of nanoparticles instead of the mesoparticles observed on HOPG. However, it is interesting to compare the electrocatalytic activity of palladium mesoparticle/HOPG and palladium nanoparticle/gold systems. The $E_{1/2}$ values derived from the voltammograms corresponding to oxygen electroreduction for palladium nanoparticles on gold are included in Figure 7. It should be noted that the electrocatalytic effect for the oerr for palladium mesoparticle/HOPG system is only slightly smaller than that observed for palladium nanoparticle/gold system. However, the former system has the advantage of no significant sintering effect of mesoscale particles and the use of a cheaper substrate.

4. Discussion

4.1. Electrocatalysis and Electrode Design. In electrocatalysis, the high performance of electrodes is the result of some combination of surface reactivity, electronic and ionic conductivity, and electron hole pair separation and facile mass transport of molecules, which is furnished by the architectural design of both electrodes in the cell, i.e., the arrangement of material in space. In electrochemical reactions the electron is a reactant

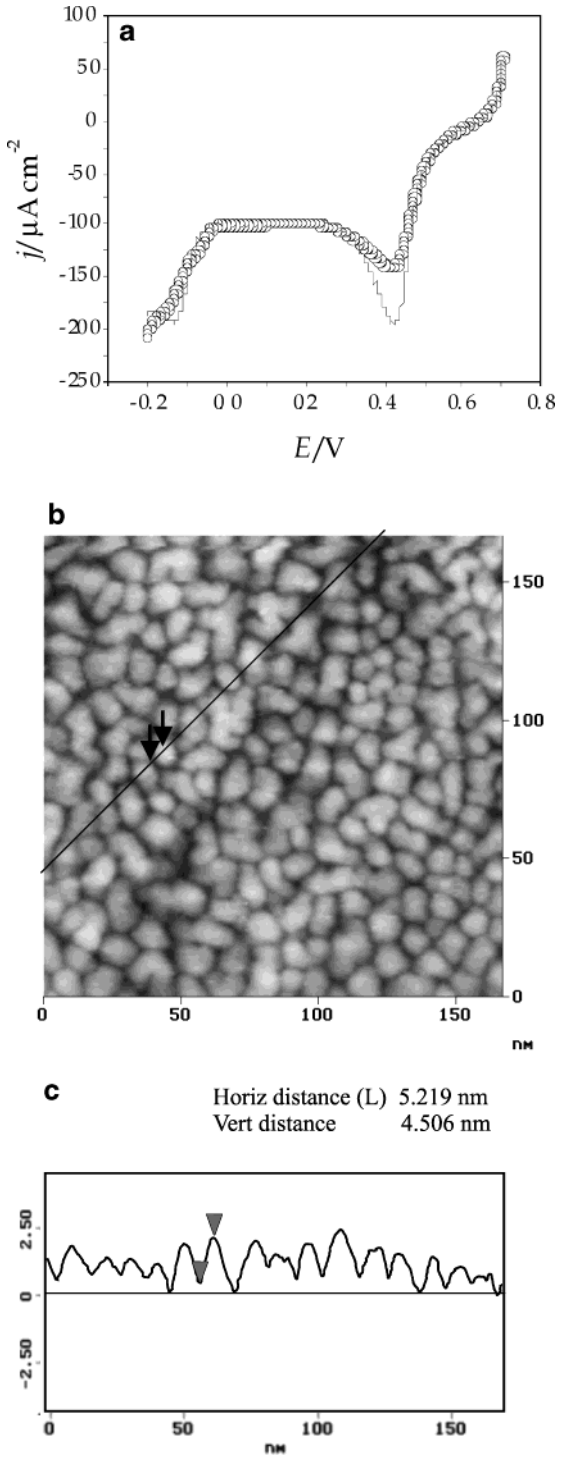

Figure 14. (a) Polarization curves in oxygen-saturated 0.05 M aqueous perchloric acid run at $v = 0.050$ V s^{-1} for the oerr on palladium nanoparticles electrodeposited on gold(111): (—) $q_d = 3$ mC cm^{-2}; (○) $q_d = 6$ mC cm^{-2}. (b) STM image (160 × 160 nm^2), $q_d = 3$ mC cm^{-2}. (c) STM cross section of the image shown in panel b.

that scales with the electrified surface area. This fact poses the issue of the optimum particle/pore size and shape of electrode materials compatible with the highest electrocatalytic activity. Accordingly, since some decades ago, these issues have become of considerable interest from the standpoint of electrochemical research.

4.2. Possible Mechanism of the oerr on Palladium Islands. The kinetics of molecular oxygen electroreduction on massive polycrystalline palladium is similar to that on massive platinum.[16] For both metals, the rate-determining step is the first single-electron-transfer step yielding adsorbed O_2^- ion from adsorbed molecular oxygen:

$$(O_2)_{ad} + e^- \rightleftharpoons (O_2^-)_{ads} \tag{2a}$$

In acid solution, reaction 2a is followed by the formation of an adsorbed O_2H radical:

$$(O_2^-)_{ad} + H^+(aq) = (O_2H)_{ads} \tag{2b}$$

The second-electron tranfer step involves the reduction of adsorbed HO_2 to adsorbed HO_2^-:

$$(O_2H)_{ad} + e^- = (HO_2^-)_{ad} \tag{2c}$$

Finally, the formation of H_2O_2 takes place:

$$(HO_2^-)_{ad} + H^+(aq) \rightarrow (H_2O_2)_{ad} \tag{2d}$$

Reactions 2a−d correspond to the first cathodic wave of molecular oxygen electroreduction on noble metals.[12−14] Therefore, H_2O_2 produced in the first electro-oxidation stage can be considered as an intermediate for the complete electroreduction of molecular oxygen.

In the second electroreduction stage, adsorbed peroxide either desorbs

$$(H_2O_2)_{ad} = H_2O_2\ (sol) \tag{3a}$$

or reacts further, yielding water:

$$(H_2O_2)_{ad} + 2H^+(aq) + 2e^- = 2H_2O(sol) \tag{3b}$$

Reaction 3b is related to the second cathodic wave for the oerr predicted from thermodynamic data (Table 1).

Previous kinetic studies have shown that the complete oerr on noble metals including palladium[13,16] involves the consecutive reaction pathway involving reactions 3a and 3b, where the first electroreduction stage behaves as an irreversible electrode process and the second one is diffusion-controlled. In contrast to massive palladium, the oerr on type I and type II palladium, under quasi-steady-state conditions, shows a limiting current that extends over a wide potential range and $E_{1/2}$ approaches the value of the reversible H_2O_2/O_2 electrode (Figure 7).

On the other hand, the experimental results also show that when the starting potential of the electroreduction curves is shifted positively, the cathodic current wave related to the oerr is also displaced in a positive potential direction (Figures 8 and 12). This fact suggests that traces of adsorbed oxygen species promote the oerr electrocatalysis. This electrocatalytic enhancement could be related to the capability of type I and type II palladium surfaces for weakening the O−O bond strength of surface species before the first electron-transfer step takes place.[16] This is not surprising because the voltammogram of palladium in the absence of dissolved molecular oxygen in the electrolyte solution (Figure 13) shows that the first electro-oxidation stage of water on palladium yielding adsorbed OH species

$$Pd + H_2O = Pd(OH) + H^+ + e^- \tag{4}$$

commences at ca. 0.3 V (Figure 13). Reaction 4 is followed by the deprotonation reaction

$$Pd(OH) = Pd(O) + H^+ + e^- \quad (5)$$

that occurs for $E > 0.5$ V (Figure 13).

Let us consider now the influence of reactions 4 and 5 on the oerr. In this case, it has been demonstrated by triangularly modulated cyclic triangular voltammetry[24] that reaction 5 behaves as a fast reversible process on noble metal electrodes. Then, the voltammetric electroreduction scan, at about 0.6 V, should involve reaction 4 in the reverse direction yielding free palladium sites. These free sites are also produced in the range 0.4−0.0 V from consecutive reactions 5 and 4, both in the reverse direction. In any case, the oerr occurs on a palladium surface partially covered by traces of OH and O adsorbates, their degree of surface coverages decreasing as the starting scanning potential is shifted negatively (Figure 13). A detailed analysis of Figures 8 and 12 definitely shows that the oerr is enhanced as the amount of OH and O adsorbates increases, irrespective of the solution composition, although this enhancement is more remarkable for reaction 3b. Correspondingly, when the starting scanning potential for the oerr is changed from 0.7 to 0.5 V, the second cathodic wave is shifted by approximately 0.2 V.

Another interesting observation is related to the appearance of the first cathodic wave related to the electroreduction of molecular oxygen to hydrogen peroxide in oxygen-free hydrogen peroxide-containing solutions (Figure 8). This wave is due to molecular oxygen produced from the hydrogen peroxide electro-oxidation during the initial anodic scan from 0.45 to 0.70 V:

$$Pd + H_2O_2 = Pd(H_2O_2)_{ad} = Pd + O_2 + 2H^+ + 2e^- \quad (6a)$$

Reaction 6a, in the reverse direction, explains the presence of the first cathodic wave under the experimental conditions described in Figure 8.

On the other hand, when the starting scanning potential for the oerr is decreased to 0.5 V, a partial oxidation of the hydrogen peroxide in the oxygen-free solution takes place according to

$$Pd + O_2H_2 = Pd(O_2H_2) = Pd(O_2H) + H^+ + e^- \quad (6b)$$

Reaction 6b, in the reverse direction, accounts for the large cathodic current recorded in the range −0.1 to −0.2 V (Figures 8 and 12). Furthermore, at these potentials the following electrochemical reaction occurs on free palladium sites

$$Pd + O_2 + e^- = Pd(O_2^-) \quad (7)$$

favoring the formation of adsorbed (O_2H)

$$Pd(O_2^-) + H^+ + e^- = Pd(O_2H)_{ad} \quad (8)$$

finally yielding hydrogen peroxide:

$$Pd(O_2H)_{ad} + H^+ + e^- = Pd(O_2H_2) \quad (9)$$

Finally, for the dissolved oxygen and hydrogen peroxide-containing solution, the electro-oxidation and electroreduction of hydrogen peroxide occur as given by reaction 6a in the forward and backward direction, respectively, and reactions 5 and 9 occurring simultaneously with those involved in the oerr reaction pathway.

4.3. Possible Explanations of the oerr Catalytic Enhancement. In heterogeneous catalysis utilizing nanometer-sized particles dispersed on high surface area oxide supports, molecular level explanations have been proposed to understand the relationships between the surface structure and size distribution of nanoparticles and their catalytic activity and selectivity.[25−29] Thus, for the catalytic conversion of carbon monooxide into carbon dioxide on gold in contact with an oxide substrate such as titania, the high performance of this system has been assigned to the reactivity of gold atoms at the perimeter of the gold/substrate contact. The number of these sites grows as the size of the particle diminishes. This high reactivity depends on the nature of the oxide support.

A second explanation for the catalytic enhancement is based upon the geometry of the gold particle. Such a particle has a smooth surface on top and lateral step edge sites where each gold atom has a higher reactivity assigned to the lesser number of gold atom neighbors. The number of this type of reactive sites also depends on the particle size.[24−27,30−33]

A third theory considers that particles smaller than 3 nm and two atomic layers thick lose their metallic properties.[30,33] Then, the high reactivity is due to the incorporation of electric charge from the substrate. This would mean that the characteristics of the substrate might also have an additional influence on the electrochemical behavior of metal islands on carbon substrates.

4.4. Topography of Palladium Island on HOPG. The shape of palladium islands potentiostatically produced on HOPG depends on E and q_c. For a fixed value of q_c, the island 2D/3D domain ratio that determines the real surface area of electrocatalytically active islands depends on E.

Let us first evaluate the increase in the total island area referred to its projection on the bare HOPG surface from the analysis of STM images by use of the Nanoscope III software. The increase in the total island area resulted in 57−60% for type I, 20−25% for type II, and 7% for type III palladium. For type II palladium, the increase in the total area comes almost entirely from the quasi-2D branched structures around island cores. For all cases, the contribution from central cores to the increase in area, as well as that from backbones left after anodic stripping, is relatively small (Figure 10c). For type III palladium, the 2D character of type II palladium has disappeared almost completely, and the corresponding pattern consists only of pseudo-1D wires of 5−8 nm in width and 3D central cores.

The large increase in total surface area observed for type I palladium results mainly from their 3D domains. In principle, one would expect that the large increase in surface area would result in a higher density of surface defects (steps, kinks, corners) and, consequently, in an enhancement of their electrocatalytic activity. However, despite the difference in surface area, the electrocatalytic effect on the oerr for type I palladium is smaller than for type II palladium. Therefore, no straightforward correlation between the enhancement of the electrocatalytic activity and the increase in the total surface area of palladium islands for the oerr can be concluded.

As a second approach to this issue, let us consider the island perimeter fractal dimension (D_s), which can be taken as a measure of the island surface disorder that would be proportional to the density number of defects. The value of D_s can be evaluated from the island perimeter/area method.[34] Accordingly, it results in $D_s = 1$ for type I palladium, $D_s = 1.4$ for type II palladium, and $D_s = 1.71$ for type III palladium. These figures show that the disorder for partially stripped islands is greater than that of type II and type I palladium. These figures change in the reverse direction to the electrocatalytic activity of these surfaces for the oerr. Then, we can conclude that on a strongly disordered perimeter that practically "fills" a plane a weakening

of the O−O bond in molecular oxygen adsorption would be unfavorable. In contrast, type II palladium exhibits the largest electrocatalytic effect for the oerr as active perimeter sites would facilitate O−O bond weakening for molecular oxygen adsorption. Finally, the less effective electrocatalytic behavior of type I as compared to type III palladium could be assigned to a smaller number of active sites at island perimeters in contact with the HOPG substrate.

On the other hand, as q_c is increased, the greater branching connectivity at type II palladium leads to percolation patterns that can be described as thin quasi-2D irregular surfaces with an average thickness of the order of 1−5 nm. These percolated electrodeposits exhibit the largest electrocatalytic effect for the oerr due to the largest density number of active sites at the irregular perimeter in relation to the isolated type II palladium observed at smaller values of q_c. Therefore, one can conclude that palladium electrodeposits with the best electrocatalytic performance for the oerr would involve an optimal density of disordered active sites at island perimeters in contact with the HOPG substrate. At these sites the weakening of the O−O bond strength at molecular oxygen adsorbates would be favored. Conversely, for hydrogen atom electroadsorption, the electrocatalytic activity appears to be similar for all types of islands suggesting that this reaction involving the participation of hydrogen atoms only takes place at all island sites.

The O−O bond strength weakening for molecular oxygen adsorbates on sites of fractal perimeter/surface palladium islands would decrease the height of the activation energy barrier associated with the first electron-transfer step. Accordingly, the first reaction step could be written as

$$2Pd^* + O_2 = [Pd^*Pd^*](O-O)_{ad} \quad (10a)$$

$$[Pd^*Pd^*](O-O)_{ad} + H^+ + 2e^- = [Pd^*Pd^*](O_2H^-)_{ad} \quad (10b)$$

$$[Pd^*Pd^*](O_2H^-)_{ad} + H^+ = 2Pd^* + H_2O_2 \quad (10c)$$

where [Pd*Pd*] stands for active centers at the palladium surface. The electroreduction of H_2O_2, either adsorbed or in solution, would further proceed via reaction 2a−d. The preceding interpretation is consistent with the fact that for clusters of atoms both the physical and chemical properties become increasingly bulklike as the cluster size increases. Then, specific structural effects determined by size-sensitive perturbation of the electronic structure, or the nature and range of interatomic interactions can arise. One special example is bond relaxation effects that give rise to a size-dependent scaling of the cluster metal−metal bond lengths.[35−38]

The palladium/oxygen interactions described in the preceding mechanism are consistent with recent quantum calculations[39,40] and agree with the likely catalytic mechanism of oxidation of carbon monoxide on gold nanoclusters on titania.[41] In this case, the formation of O_2^- species at 673 K was detected by electron spin resonance.[42,43] From the figures given above, one can conclude that the origin of the electrocatalysis for the oerr is related to the fractal perimeter of palladium islands rendering a large number of local defect sites at the HOPG surface/palladium island edges/electrolyte solution three-phase boundaries. This fact implies a considerable influence of the substrate characteristics on the electrocatalytic properties of metal island/substrate systems. Actually, the influence of carbon substrates on the electrocatalysis for redox reactions by metal nanoparticles have been recently reported.[44]

5. Conclusions

The catalytic activity of palladium islands on HOPG is surprisingly high at the level of the first electron-transfer step. This process at palladium mesoparticles would be assisted by a weakening of the O−O bond strength at molecular oxygen adsorbates. Our results suggest that different features of the electrochemical system converge to produce the above-mentioned electrocatalytic effect. The fractal perimeter of islands that leads to an increase in the number of active sites at island perimeters, the effective area of working electrodes, and the influence of traces of oxygen-containing surface species remaining on the palladium island surface seem to cooperate to produce a faster dissociation of molecular oxygen undergoing together with the first electron-transfer step in the oerr.

Considering the different explanations advanced for the catalytic enhancement promoted by metal particles on solid substrates, the electrocatalytic effect of type I and type II palladium for the oerr first results from the number of highly reactive palladium atoms at island edges in contact with the HOPG substrate. The number of atoms at island edges in contact with the substrate is greater for type II than for type I palladium. Traces of oxygen-containing adsorbates on palladium islands also contribute to promote the electrocatalytic effect. The dissociative adsorption of molecular oxygen at the preferred sites reduces the activation energy barrier for the first electron-transfer step in the oerr mechanism. The dissociative adsorption is hindered for extremely disordered systems as observed for type III palladium. The palladium mesoparticle/HOPG system exhibits an electrocatalytic behavior comparable to that of the palladium nanoparticle/gold system.

Acknowledgment. This work was financially supported by projects PICT 98 06-03251 from the Agencia Nacional de Promoción Científica y Tecnológica (Argentina), BQU2000-0247 and BQU2002-03249 from the Ministerio de Ciencia y Tecnología (Spain), and the CSIC/CONICET cooperation programm. R.C.S. thanks the Dirección General de Investigación Científica y Enseñanza Superior (Spain).

References and Notes

(1) Bockris, J. O.'M.; Khan, S. U. *Surface Electrochemistry. A Molecular Level Approach*; Plenum Press: New York, 1993.
(2) Pletcher, D.; Walsh, F. C. *Industrial Electrochemistry*; Chapman and Hall: London, 1990.
(3) Mahé, E.; Devilliers, D. *Electrochim. Acta* **2000**, *46*, 629.
(4) Haruta, M.; Daté, M. *Appl. Catal. A* **2001**, *222*, 427.
(5) Favier, F.; Walter, E. C.; Zach, M. P.; Benter, T.; Penner, R. M. *Science* **2001**, *293*, 2227.
(6) Kravtsov, V. I.; Zelenskii, M. I. *Elektrokhimiya* **1965**, *2*, 1138.
(7) Kolyadko, E. A.; Shigan, L.; Pdlovchenko, B. I. *Elektrokhimiya* **1992**, *28*, 385.
(8) Podlovchenko, B. I.; Kolyadko, E. A.; Shigan, L. *J. Electroanal. Chem.* **1995**, *399*, 21.
(9) Rusanova, M. Yu.; Tsirlina, G. A.; Petrii, O. A.; Safonova, Ya.; Vasiliev, S. Yu. *Russ. J. Electrochem.* **2000**, *36*, 457.
(10) Walter, E. C.; Favier, F., Penner, R. M. *Anal. Chem.* **2002**, *74*, 1546.
(11) Gimeno, Y.; Hernández Creus, A.; González, S.; Salvarezza, R. C.; Arvia, A. J. *Chem. Mater.* **1999**, *13*, 1857.
(12) Gimeno, Y.; Hernández Creus, A.; Carro, P.; González, S.; Salvarezza, R. C.; Arvia, A. J. *J. Phys. Chem. B* **2002**, *106*, 4232.
(13) Sawyer, D. T. *Oxygen Chemistry*; Oxford Univesity Press: New York, 1991.
(14) Hoare, J. P. *J. Electrochem. Soc.* **1963**, *110*, 1019.
(15) Hoare, J. P. *J. Electrochem. Soc.* **1965**, *112*, 1129.
(16) Hoare, J. P. *The Electrochemistry of Oxygen*; Interscience Publishing: New York, 1968.
(17) Sobol, V. V.; Kruskcheva, E. I.; Dagaeva, V. A. *Elektrokhimiya* **1965**, *1*, 1332.
(18) El-Daeb, M. S.; Ohsaka, T. *Electrochem. Commun.* **2002**, *4*, 288.
(19) El-Daeb, M. S.; Ohsaka, T. *Electrochim. Acta* **2002**, *47*, 4255.

(20) Zhang, Y.; Ashahina, S.; Yoshihara, S.; Shirakashi, T. *Electrochim. Acta* **2003**, *48*, 741.
(21) Kessler, T.; Visintin, A.; Bolzan, A. E.; Andreasen, G.; Salvarezza, R. C.; Arvia, A. J. *Langmuir* **1996**, *12*, 6587.
(22) Andreasen, G.; Visintin, A.; Salvarezza, R. C.; Triaca, W. E.; Arvia, A. J. *Langmuir* **1999**, *15*, 1.
(23) Bard, A. J., Parsons, R., Jordan, J., Eds. *Standard Potentials in Aqueous Solution*; IUPAC/M. Dekker: New York and Basel, Switzerland, 1985.
(24) de Tacconi, N. R.; Zerbino, J. O.; Arvia, A. J. *J. Electroanal. Chem.* **1977**, *79*, 287.
(25) Koresh, J.; Soffer, A. *J. Electrochem. Soc.* **1997**, *124*, 1379.
(26) Valden, M.; Lai, X.; Goodman, D. M. *Science* **1998**, *281*, 1698.
(27) Rolison, D. R. *Science* **2003**, *299*, 1698.
(28) Bell, A. T. *Science* **2003**, *299*, 1685.
(29) Hernández Creus, A.; Salvarezza. R. C.; Arvia, A. J. *Encyclopedia of Nanoscience and Nanotechnology*; Nalwa, E., Ed.; American Scientific Publisher: New York, 2003.
(30) Mavrikakis, M.; Stoltze, P.; Norskov, J. *Catal. Lett.* **2000**, *64*, 101.
(31) Olea, M.; Kunitake, M.; Shido, T.; Iwasawa, J. *Phys. Chem. Chem. Phys.* **2001**, *197*, 627.
(32) Arvia, A. J.; Triaca, W. E.; Salvarezza, R. C. *J. New Mater. Electrochem. Syst*., in press.
(33) Penner, R. M. *J. Phys, Chem. B* **2002**, *106*, 3339.
(34) Gómez-Rodríguez, J. M.; Baró, A. M.; Vázquez, L.; Salvarezza, R. C.; Vara, J. M.; Arvia, A. J. *J. Phys. Chem*. **1992**, *96*, 347.
(35) Seri-Levy, A.; Avnir, D. *Surf. Sci.* **1991**, *248*, 258.
(36) Sinfelt, E.; Via, G. H.; Lytle, F. W. *J. Chem. Phys.* **1978**, *68*, 2009.
(37) El-Sayed, M. A. *Acc. Chem. Res.* **2001**, *34*, 257.
(38) Frenkel, A. I.; Hills, C. W.; Nuzzo, R. G. *J. Phys. Chem. B* **2001**, *105*, 12689.
(39) García-Rodeja, J.; Rey, C.; Gallego, L. J.; Alonso, J. A. *Phys. Rev. B* **1994**, *49*, 8495.
(40) Karabacak, M.; Ozcelik, S.; Guvenc, Z. V. *Surf. Sci.* **2002**, 507−510, 636.
(41) Roques, J.; Lacaze-Dufaure, C.; Mijoule, C. *Surf. Sci.* **2001**, *479*, 231.
(42) Liu, H.; Kozlov, A.; Kozlova, A.; Shido, T.; Asakura, K.; Iwasawa, Y. *J. Catal.* **1999**, *185*, 252.
(43) Schubert, M. M.; Hackenberg, S.; van Veen, A.; Muhler, M.; Plzak, V.; Behm, R. *J. Catal.* **2001**, *197*, 113.
(44) Mayer, P.; Holze, R. *J. Solid State Electrochem.* **2001**, *5*, 402.